# Simulation of Retrofitted Unreinforced Concrete Masonry Unit Walls under Blast Loading

**Sanam Aghdamy, Chengqing Wu* and Michael Griffith**
School of Civil, Environmental, and Mining Engineering, The University of Adelaide, Australia

(Received date 2 Jan 2012; Accepted date 14 Dec 2012)

ABSTRACT
This paper describes an investigation into the effectiveness of using spray-on nano-particle reinforced polymer and aluminium foam as new types of retrofit material to prevent the breaching and collapse of unreinforced concrete masonry walls subjected to blast over a whole range of dynamic and impulsive regimes. Material models from the LS-DYNA material library were used to model the behaviors of each of the materials and its interface for retrofitted and unretrofitted masonry walls. Available test data were used to validate the numerical models. Using the validated LS-DYNA numerical models, the pressure-impulse diagrams for retrofitted concrete masonry walls were constructed. The efficiency of using these retrofits to strengthen the unreinforced concrete masonry unit (CMU) walls under various pressures and impulses was investigated using pressure-impulse diagrams. Comparisons were made to find the most efficient retrofits for masonry walls against blasts.

**Key words:** Airblast loads; Aluminium foam; Nano-particle reinforced polymer; Concrete masonry; Pressure-impulse diagram

## 1. INTRODUCTION

Structural frames infilled with unreinforced concrete masonry unit walls are very common all over the world. CMU walls are frequently used in buildings because they offer a cost-effective option and can satisfy many building requirements; however, they are extremely susceptible to blast pressure, resulting in wall collapse, fragmentation, and severe injury to occupants (Wu, Hao 2007; Moradi 2007; Hao, Tarasov 2008; Wang, Hao, Ding, Li 2009; Moradi, Dinan, Bewick, Davidson 2011; Bazhenov, Kibetz, Kruszka 2012). Consequently, there is a need to retrofit CMU walls to increase their resistance to blast loading.

Conventional retrofitting methods focus on increasing the overall strength of the structure by adding steel or concrete, which is time consuming and expensive (Islam 2008; Stone and Engebretsen 2006). New retrofit techniques that focus on increasing the ductility of wall elements rather than strengthening them include the application of fiber reinforced polymer (FRP) platting; unreinforced elastometric materials, such as spray-on and trowel-on

*Corresponding author. *E-mail address:* cheng.wu@adelaide.edu.au

polyureas; reinforced elastometric materials, such as spray-on reinforced polyurea; metallic foam cladding; or a combination of these techniques (Davidson, Fisher, Hammons, Porter, Dinan 2005; Al-Ostaz, Cheng, Mullen, Mantena 2009).

Myers, Belarbi, El-Domiaty (2004) experimentally examined the efficiency of using FRP for the protection of masonry buildings against blast loads. They concluded that FRP composites offer great benefits in terms of strengthening masonry walls to resist blast loads. Furthermore, the composites also increase the out-of-plane flexural capacity of walls to withstand a variety of other threats. Research indicates, nevertheless, that the performance of FRP is limited by its interaction with the masonry (Myers , Belarbi, El-Domiaty 2004; Lunnand and Rizkalla 2011), and that debonding failure commonly occurs at the interface of the two materials.

In the light of this problem, Davidson and Moradi (2004) investigated the effectiveness of using spray-on polymers to improve the blast resistance of unreinforced masonry walls. Full-scale explosive tests conducted by these researchers indicated that the polymer can bond to the masonry wall, forming a tough elastic skin. Although the polymer tore at a mortar joint near the middle of the wall as it flexed, all of the wall panels remained intact and prevented debris from penetrating into the structure.

The potential benefits of using both reinforced and unreinforced polymers to retrofit hollow, unreinforced, concrete masonry walls were investigated by Johnson, Slawson, Cummins, and Davis in 2005. Results of their investigation suggested that unreinforced polymer did add minor additional flexural resistance to hollow, unreinforced CMU walls. However, the addition of reinforcement to the polymer retrofit system significantly increased the flexural resistance of the walls.

More recent blast tests by the nano-infrastructure research group at the University of Mississippi on $\frac{1}{4}$-scale CMU walls retrofitted with nano-particle reinforced polyureas (NPRPs) indicated that NPRPs can significantly enhance the ductility and resilience of masonry wall systems. Their large strain capacity can be exploited to absorb blast energy and contain building debris (Al-Ostaz, Cheng, Mullen, Mantena 2009).

Whilst polyurea has the advantage of high elongation capability, high shear strength capacity, easy application, quick cure and availability for purchasing at an acceptable cost (Knox, Hammons, Lewis, Porter 2000), the introduction of nano-reinforcement could further enhance its overall material performance (Krishnamoorti and Vaia 2001; Vaia 2003). The main advantages of nano-reinforcement are summarized in the work of Griffith (Griffith 1920) and Weibull (Weibull 1951). Both researchers, many years apart, reported that the smaller a material is, the stronger it becomes, assuming that the failure of macroscopic specimens is due to the existence of defects (i.e., cracks), and that materials that are smaller than a critical crack length are able to reach their theoretical maximum strength (Griffith 1920; Weibull 1951).

A nano-material currently being investigated is the exfoliated graphite nano-platelet (xGnP), a type of conventional nano-platelet composite in which graphite exists as a layered material with the layers held together by van der Waals forces. xGnP exhibits large intrinsic fracture energy and can undergo a considerable out-of-plane deformation before fracture (Irshidat 2010). When used in composites, this nano-platelet material may improve surface toughness, stiffness and tensile strength (Krishnamoorti and Vaia 2001).

Since the late 1990s, research has suggested that xGnP could be used as a nano-reinforcement in polymer systems (Irshidat 2010), given the ability of graphite to exfoliate through graphite intercalated compounds (GICs). Furthermore, natural graphite is abundant and its cost is low compared to the other nano-sized carbon materials (Irshidat 2010).

Alternatively, a class of silicon based nano-chemicals has recently been hailed as the next big leap in nano-material technology. Polyhedral oligomeric silsesquioxane (POSS) is a highly cost competitive silicon-based nano-chemical that can be incorporated into

polymers to produce significant improvements in their mechanical and thermal resistance. There is evidence that its addition increases the impact resistance and self-healing capabilities of polymers (Irshidat 2010). Research has been limited, however, into the overall effectiveness of POSS (Al-Ostaz, Cheng, Mullen, Mantena 2009; Su 2008; Su, Wu, Griffith 2011).

In addition to novel nano-technologies, aluminium foam has also been investigated as a retrofit due to its excellent mechanical properties, relative low cost and high energy absorption capability, all of which can be used to mitigate the effects of an explosive load on a structural system (Hanssen, Enstock., Langseth 2002; Montanini 2005; Wu, Huang, Oehlers 2010). The typical behaviour of aluminium foam in uniaxial compression is illustrated in Figure 1 (CYMAT 2003).

As highlighted by the figure, aluminium foam in compression resembles a perfect plastic material, which makes it very attractive for use as a sacrificial layer for blast protection. Aluminium foam can prolong the duration of a blast load and reduce the peak pressure impacting on the contact surface between the foam and the protected structural member (Hanssen, Enstock, Langseth 2002; Wu, Huang, Oehlers 2010). Schenker, Anteby, Nizri (2005) and Wu, Huang, Oehlers (2010) investigated the capability of aluminium foam to protect RC slabs subjected to blast loading. The results of field tests revealed that aluminium foam is very effective in absorbing blast energy for RC slabs. It is believed that aluminium foam is also very effective in absorbing blast energy for CMU walls (Su 2008).

Pressure-impulse (P-I) diagrams have been widely used to evaluate the effectiveness of materials designed to protect structures against a wide range of reflected pressures with different durations, and two current standards advocate their usage (UFC 2008; ASCE 1997). P-I diagrams can assist investigations into the effectiveness of retrofits in various regimes (i.e., impulsive, dynamic and quasi-static regimes) by comparing the unretrofitted response with the retrofitted response. At the same time, they also help to understand the influence of various retrofitting design parameters on the performance of the structure under different pressures and impulses.

Although the development of P-I diagrams should be based on the actual behavior of the structure under blast loading, the high cost of blast tests makes this impractical. Furthermore, the short duration and destructive nature of an explosion mean that it is difficult to determine structural responses only through experimental testing. It is necessary, therefore, to rely on computational techniques using finite element software, such as LS-DYNA, to derive P-I curves.

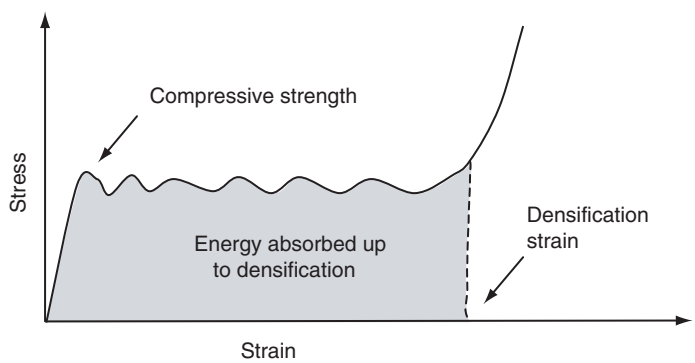


Figure 1. Schematic stress- strain curve of aluminium foam (CYMAT 2003)

The main objectives of the present study were, therefore: (1) to develop accurate numerical models to simulate the response of CMU walls retrofitted with sprayed-on NPRP and aluminium foam, respectively; (2) to investigate the effectiveness of using sprayed-on NPRP and aluminium foam as retrofits on a CMU wall by utilizing numerically developed P-I diagrams; and (3) to assess the influence of various retrofitting design parameters on the effectiveness of these retrofit materials with the aid of P-I curves.

## 2. NUMERICAL MODELLING OF RETROFITTED CMU WALLS

The focus of the first part of the research was the development of models that could replicate with reasonable accuracy the failure mechanism and midpoint deflection of retrofitted CMU walls subjected to blast loads. These models were then used to derive P-I diagrams in order to evaluate the viability of using spray-on NPRP and aluminium foam to protect the unreinforced CMU. A comprehensive description of the modeling methodology is provided in Aghdamy (2010).

### 2.1. MATERIAL MODELS

#### *2.1.1. Concrete Masonry Wall*

In the current study, the hollow concrete block and mortar were discretized and modeled individually using an eight-node solid element. For analysis of concrete walls, LS-DYNA provides a variety of constitutive models (material cards) simulating numerous behavior patterns. However, MAT_SOIL_AND_FOAM (material type 5) was selected to model both the hollow concrete block and mortar based on the recommendation made in Davidson and Moradi (2004), who had evaluated several material models – MAT_SOIL_AND_FOAM, MAT_BRITTLE_DAMAGE, MAT_PSEUDO_TENSOR, and MAT_WINFRITH_CONCRETE – for simulating the hollow concrete block and mortar. The researchers concluded that MAT_SOIL_AND_FOAM best correlated with test data obtained from field tests. It is also the simplest model and closely matches the common hollow concrete block composed of plain concrete material exhibiting simple fracture modes (Moradi, Davidson, Dinan 2008).

As the model is one of the constitutive models in LS-DYNA which does not allow for failure and erosion, the MAT_ADD_EROSION option in LS-DYNA was employed to provide a way of including failure in the model. The principal strain criterion was used as the failure criterion for hollow concrete block and mortar and the element was deleted from the calculation when the principal strain in the element reached the failure criterion.

The defined yield criterion was based on Drucker-Prager strength theory. The Drucker-Prager yield criterion is given by:

$$\alpha I_1 + \sqrt{J_2} - k = 0 \tag{1}$$

where $J_2$ is the second invariant of the deviatoric stress tensor $S_{ij}$; $I_1$ is the first invariant of the stress tensor, given by $J_2 = 0.5\ S_{ij}S_{ij}$; $I_1 = (\sigma_{11} + \sigma_{22} + \sigma_{33})$; $\alpha$ is the pressure sensitivity coefficient; and $k$ is a material constant, which can be determined by:

$$\alpha = \frac{m-1}{\sqrt{3(m+1),}} \quad k = \frac{2\sigma_c}{\sqrt{3}(m+1)} \tag{2}$$

where $m = \sigma_c/\sigma_t$, $\sigma_t$ and $\sigma_c$ are the maximum stresses in uniaxial tension and compression, respectively.

In the current study, the CMU wall was identical to one used in a comprehensive investigation performed by the nano-infrastructure research group at the University of Mississippi, jointly with US Army Engineering Research and Development Center (ERDC). The main goal of the university and the ERDC researchers was to assess advanced materials for the protection of critical infrastructure against terrorist threats (Al-Ostaz, Cheng, Mullen, Mantena 2009).

The model is a quarter-scale wall made of scaled down concrete blocks. The wall is 16 blocks high (906 mm) and 12 blocks long (1411 mm) (Figure 2). It was cast in a steel frame with dowels set at top and bottom to simulate simply supported conditions along the top and bottom edges and free boundary conditions along its vertical edges. The masonry unit is a hollow concrete block with the outside dimensions of 115 mm × 57 mm × 54 mm with hole sizes of 46 mm × 38 mm × 54 mm. A mortar joint of thickness 2.8 mm was assumed in the scaled model. Figure 3 shows the numerical model of the CMU unit.

A convergence test was conducted to choose the element size. This involved continually halving the element size in the numerical model until a 5% difference in the numerical results was achieved. The basic material properties of the concrete block and mortar which were used to model the wall are presented in Tables 1 and 2, respectively.

Table 3 lists the values of material constants $\alpha$ and $k$ in Eqn (1) for the concrete block and mortar used in this study. It should be noted that the strain rate effects on the concrete block and mortar properties were not taken into account here.

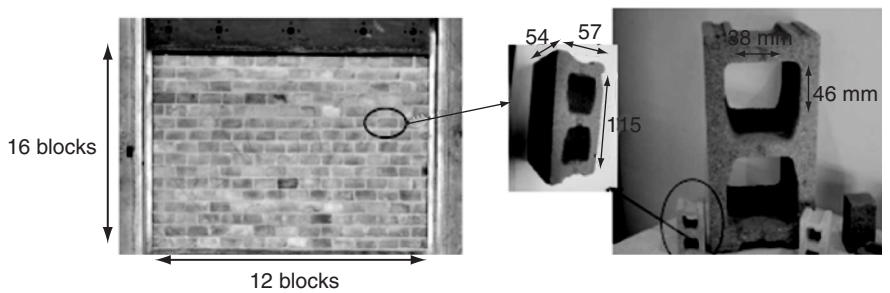


Figure 2. The adopted CMU model (Moradi 2003)

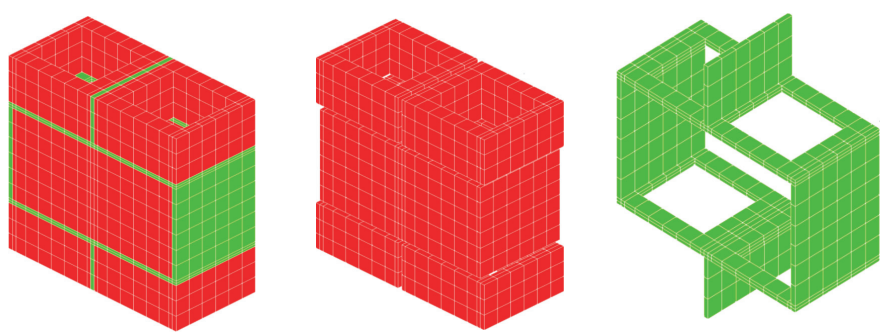


Figure 3. Finite element model of the concrete masonry unit

Table 1. Material properties of hollow concrete block (Moradi 2003)

| **Parameter** | **Value** |
|---|---|
| Mass density (kg/m$^3$) | 1921 |
| Ultimate compressive strength (MPa) | 13.8 |
| Ultimate tensile strength (MPa) | 1.4 |
| Young's modulus (GPa) | 12.5 |
| Shear modulus (GPa) | 5.4 |
| Poisson's ratio | 0.15 |

Table 2. Material properties of mortar

| **Parameter** | **Value** |
|---|---|
| ***Given properties*** (Al-Ostaz, Cheng, Mullen, Mantena 2009) | |
| Mass density (kg/m$^3$) | 1921 |
| Ultimate compressive strength (MPa) | 12.4 |
| **Assumed properties (Moradi 2003)** | |
| Ultimate tensile strength (MPa) | 1.55 |
| Tensile bond strength (MPa) | 0.35 |
| Young modulus (GPa) | 5.8 |
| Shear modulus (GPa) | 2.2 |
| Poisson's ratio | 0.33 |

Table 3. Material constants $\alpha$ and $k$ in Eqn (1) used for the concrete block and mortar

| **Material** | ***m*** | $\alpha$ | ***k* (MPa)** |
|---|---|---|---|
| Concrete block | 10 | 0.47 | 1.5 |
| Mortar | 8 | 0.45 | 1.6 |

### *2.1.2. NPRPs*

The NPRP coatings were modeled using the eight-node solid element in LS-DYNA. To determine a suitable material model for simulating the polymer reinforcement behavior, the polymer elements were then tied to the block and mortar elements using a contact interface. The criteria to determine a suitable material model for simulating the polymer reinforcement behavior include: (1) having an appropriate failure condition to simulate rupture; (2) having the ability to be modeled with solid elements; and (3) being applicable to plastic and/or elastomeric behavior.

Of the material models considered – MAT_PLASTIC_KINEMATIC (material type 3), MAT_PIECEWISE_LINEAR_PLATICITY (material type 24) andMAT_RATE_SENSITIVE_POLYMER (material type 141) – material model 3 allowed for the most appropriate material fracture without computational problems. Because it also satisfied the defined criteria while requiring fewer inputs where limited material properties were available, this material card was selected.

Polymers reinforced by xGnP from XG-Sciences and POSS from Hybrid Plastics Inc. were used in the current research. The polymer used for retrofitting consisted primarily of polyurea line-XS 350 produced by Protective Coatings Inc. Figure 4 shows typical stress-strain

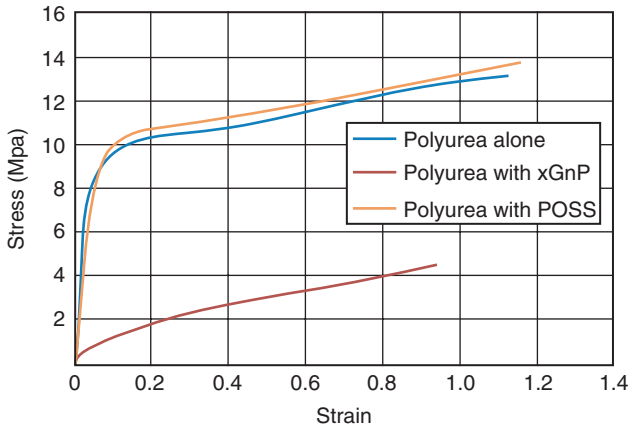


Figure 4. Typical stress-strain relationship for retrofitted materials under tensile loading (Al-Ostaz, Cheng, Mullen, Mantena 2009)

Table 4. Average material properties of xGnP reinforced polyurea and POSS reinforced polyurea (Al-Ostaz, Cheng, Mullen, Mantena 2009)

| Material | Young's Modulus (MPa) | Poisson's Ratio | Ultimate Strength (MPa) | Strain at Rupture (%) |
|---|---|---|---|---|
| Polyurea with xGnP | 12.9 | 0.4 | 4.5 | 96 |
| Polyurea with POSS | 199.8 | 0.4 | 13.5 | 116 |

curves obtained from standard uni-axial direct tensile tests for each specimen of unreinforced polyurea, xGnP reinforced polyurea, and POSS reinforced polyurea. These quasi-static tests were conducted by Al-Ostaz, Cheng, Mullen, Mantena (2009) at ERDC.

The stress-strain curves in the figure indicate that adding POSS particles to polyurea slightly *increases* the ductility and strength of the unreinforced polyurea. However, adding xGnP particles *reduces* the ductility and strength of the unreinforced polyurea. Table 4 provides the key average mechanical characteristics of these materials. The strain rate dependent properties were obtained from Al-Ostaz, Cheng, Mullen, Mantena (2009).

Figure 5a and Figure 5b show strain rate dependent stress versus strain curves that were used in the xGnP reinforced polyurea and POSS reinforced polyurea models. The thickness of the xGnP reinforced polyurea and POSS reinforced polyurea were set at 1.5 mm and 1.8mm, respectively.

### *2.1.3. Aluminium Foam and Steel Cover*

The aluminium foam and steel cover were modelled using eight-node solid elements in LS-DYNA. The numbering convention of material directions is shown in Figure 6. Since the foam has a natural directionality, the material model was selected carefully to replicate the real anisotropic behavior of the foam. Of the two models – MAT_HONEYCOMB (material type 26) and MAT_MODIFIED_HONEYCOMB (material type 126) – developed in LS-DYNA for foam material with anisotropic behavior, material model 126 was selected. This

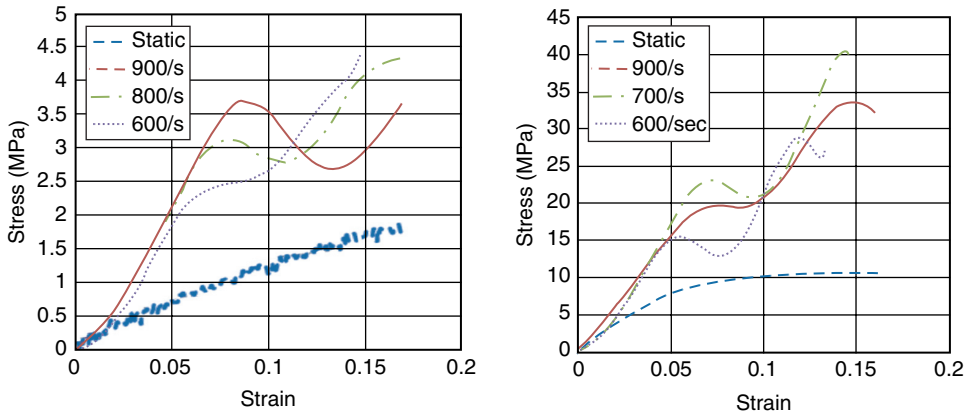


Figure 5. Stress-strain relationship for NPRPs under dynamic tensile loading (Al-Ostaz, Cheng, Mullen, Mantena 2009)

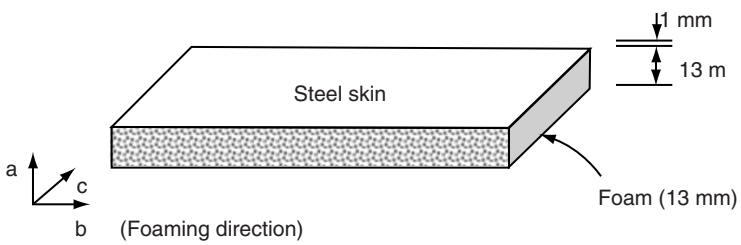


Figure 6. Numbering convention of foam material directions

model, which allows nonlinear elastoplastic material behavior to be defined separately for all normal and shear stresses, is a modified version of material model 26. It differs from material type 26 in the history dependency (description of hardening) of the yield surface. Some element formulations are applicable only to material model 126, accounting for severe element distortions.

The facesheet, which protects the aluminium foam from disintegration, is made of steel. Since steel is an elasto-plastic material, it was modelled using material card MAT_PLASTIC_KINEMATIC (material type 3).

In this study, A356SiC040, which is a closed cell aluminium foam produced by CYMAT Corporation, was used. Table 5 and Table 6 list the basic material properties for the A356SiC040 foam and steel cover respectively.

Using the nonlinear elastoplastic material model 126 in LS-DYNA, a compressive test of an aluminium foam specimen (A356SiC040) with a length of 400 mm, a width of 400 mm and a thickness of 40 mm was simulated. Figure 7 compares the stress-strain curve obtained from an actual compressive test on the aluminium foam specimen (A356SiC040). It is clear that the simulated results agree well with the experimental data. Similarly the numerical results in 'b' and 'c' directions also agree well with the test data, indicating that the performance of the aluminium foam sheet can be effectively simulated with the nonlinear

Table 5. Material properties of aluminium foam A356SiC040 (CYMAT 2003)

| **Parameter** | **Value** |
|---|---|
| Poisson's ratio | 0.33 |
| Tensile stress in a direction (MPa) | 3.2 |
| Tensile stress in b direction (MPa) | 3.7 |
| Tensile stress in c direction (MPa) | 5.0 |
| Tensile modulus in a direction (GPa) | 1.2 |
| Tensile modulus in b direction (GPa) | 1.3 |
| Tensile modulus in c direction (GPa) | 1.5 |
| Compressive strength in a direction (MPa) | 4.0 |
| Compressive strength in b direction (MPa) | 5.0 |
| Compressive strength in c direction (MPa) | 6.0 |
| Compressive modulus in a direction (GPa) | 0.5 |
| Compressive modulus in b direction (GPa) | 0.7 |
| Compressive modulus in c direction (GPa) | 0.85 |
| Shear strength (MPa) | 2.1 |
| Shear modulus (GPa) | 0.92 |
| Densification strain (%) | 68 |

Table 6. Material properties of steel cover

| **Parameter** | **Value** |
|---|---|
| Poisson's ratio | 0.28 |
| Yield strength (MPa) | 300 |
| Elastic modulus (GPa) | 207 |
| Density (kg/m$^3$) | 7830 |

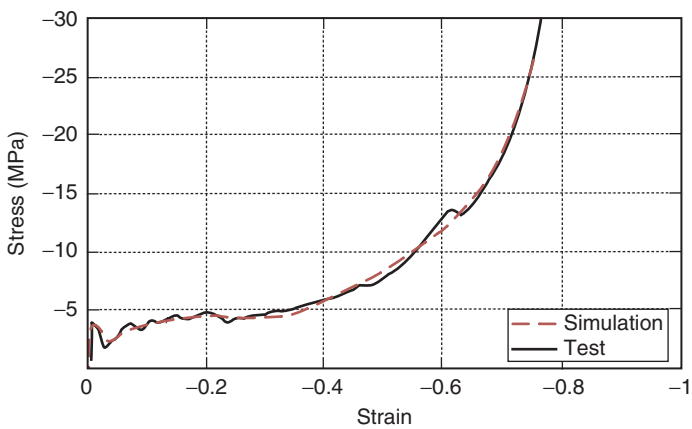


Figure 7. Comparison of compressive stress-strain curves between simulation and test in direction 'a' (Su 2008)

elastoplastic material model. Thus it can be assumed that this material model is also suitable for blast loading.

## 2.2. CONTACT SURFACE MODEL

The masonry and aluminium foam were considered to be connected initially by the contact nodes. It was assumed that these bonds broke once the failure stress criterion specified by Eqn (3) was reached:

$$\left(\frac{|\sigma_n|}{\sigma_{ft}}\right)^2 + \left(\frac{|\tau_s|}{\tau_f}\right)^2 \geq 1 \tag{3}$$

where $\sigma_n$ and $\tau_s$ are the normal and shear stresses while $\sigma_{ft}$ and $\tau_f$ are the ultimate normal and shear stresses of the contact surfaces, respectively. The damage was defined as a linear function of deformation between the nodes that were initially in contact. After stress $\sigma_n$ or $\tau_s$, or their combination, attained the ultimate levels of stress, damage occurred and stress was scaled by the linear damage function. When the deformation increased to the critical failure slip $\delta_f$, the damage was complete and the contacts failed.

After failure, only friction was considered between the parts that had initially been in contact. Assuming no load reversal, the energy released rate due to the failure of the interface was approximately $0.5 \times S \times \delta_f$ where $S$ can be computed from Eqn (4) at the initiation of damage:

$$S = \sqrt{\max(\sigma_n, 0)^2 + |\sigma_s|^2} \tag{4}$$

The 'CONTACT_AUTOMATIC_SINGLE_SURFACE' card in LS_DYNA was used to define the interface contact between the steel facesheet of the aluminium foam and a masonry wall, with $\tau_f$ taken as 7.8 MPa and $\sigma_{ft}$ equal to be the tensile strength of the concrete block, 1.4 MPa (Al-Ostaz, Cheng, Mullen, Mantena 2009; Su 2008).

It should be noted that the same contact type which is based on normal and shear strength failure parameters, with $\tau_f$ taken as 0.35 MPa and $\sigma_{ft}$ taken as equal to the tensile strength of the mortar, 1.6 MPa, was used to model the strength of the concrete block-mortar bond. Therefore, the same expression as in Eqn (3) can be used.

## 2.3. BOUNDARY CONDITIONS

The support conditions were defined carefully as they were one of the main parameters in determining the strength and fracture behavior of the CMU wall. The BOUNDARY_SPC option in LS-DYNA was used to restrain translational displacement in all directions along the top and bottom edges of the ungrouted wall. In this way simply supported conditions along these edges were simulated. Vertical edges remained unrestrained in accordance with the type of CMU wall that was adopted (Al-Ostaz, Cheng, Mullen, Mantena 2009).

## 2.4. EXPERIMENTAL VALIDATION OF NUMERICAL SIMULATIONS

Prior to the employment of the numerical models for the development of the P-I diagrams, it was necessary to validate the models with an experiment. For the purposes of the current

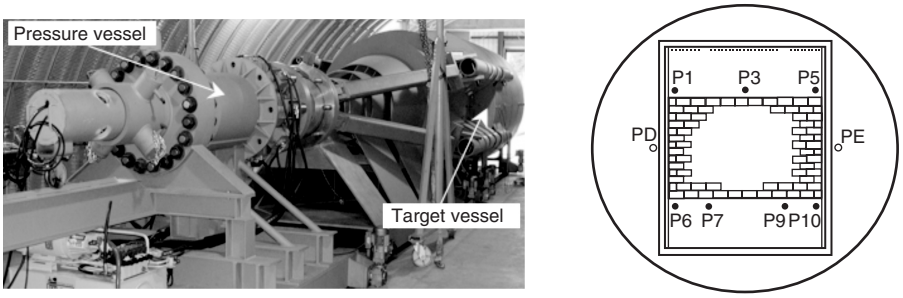


(a) Blast simulator (b) Location of pressure sensors

Figure 8. Blast experiments at ERDC (Moradi 2003)

research, the results of blast experiments performed on three different quarter-scale retrofitted CMU walls at the ERDC were adopted (Al-Ostaz, Cheng, Mullen, Mantena 2009). The CMU walls had the same dimensions and properties as defined in section 2.1. Each wall was cast in a steel frame with dowels at top and bottom to simulate simply supported conditions and free boundary conditions on the left and right.

### 2.4.1. Experimental Data

In the experiments, pre-adjusted air blast pressure and impulse were applied to each wall using a blast simulator (BLS) (Figure 8a). Pressure time histories were obtained by nine pressure sensors mounted on the steel loading frame (Figure 8b). Mid-point deflection for each wall was obtained by the integration of the recorded data collected from an accelerometer.

### 2.4.2. Unretrofitted CMU Wall

The numerical model of the unretrofitted CMU wall was initially validated for its soundness by comparing LS-DYNA mid-height displacement results at cracking and instability with those of analytical predictions under ultimate static load. Following validation, the model's maximum midpoint deflection and its failure shape were compared with results obtained from blast experiments.

For a simple-supported CMU wall undergoing vertical bending, the wall initially behaves elastically. This elastic behavior of the wall continues until the wall reaches its ultimate bending capacity, and cracking starts to occur at a bed joint near the wall's mid-height. The post cracking behavior of the wall is then non-linear. Under deflection control loading, the wall collapses when the mid-height deflection exceeds the point of instability (Willis 2004). The displacement at the onset of cracking can be determined by Eqn (5):

$$\Delta_{cr} = \frac{5P_{ult}h^4}{384EI} \tag{5}$$

where $E$ is Young's modulus of masonry; $I$ is the second moment of area; $h$ is the wall height; and $P_{ult}$ is the ultimate static lateral load which an unretrofitted wall can resist and given by $P_{ult} = 8M_{cv}/h^2$. $M_{cv}$ is the wall's vertical bending moment capacity and was computed using Eqn (6):

$$M_{cv} = (f'_{mt} + f_d)Z_d \tag{6}$$

where $f_d$ is design compressive stress on the bed joint due to the vertical force acting on the bed joint under consideration; $f_{mt}$ is the flexural tensile strength of the masonry; and $Z_d$ is the section modulus of the cross-section. The deflection at instability of a simply supported wall can be estimated from the one-way vertical bending theory derived by Willis (2004);

$$\Delta_{ult} = t\left[1 - \frac{\sigma v + 0.25\,\rho g h}{f_{mc}}\right] \tag{7}$$

where $t$ is the thickness of the CMU wall; $\sigma_v$ is the pre-compressive stress on the bed jointp; $\rho$ is the mass density of the CMU wall; $g$ is the gravitational acceleration; $f_{mc}$ is the ultimate compressive strength of the masonry; and $h$ is the wall height. At the ultimate static pressure of 1.4 kPa, difference of the estimated displacement at cracking using the analytical method and LS-DYNA simulation is 5.1%. Furthermore, the analytical method estimated the displacement at instability to be 57 mm which has an approximately 6% difference with the result obtained from LS-DYNA.

Whilst the numerical model of the unretrofitted wall was checked for its accuracy using the analytical estimations, the soundness of the model was confirmed when the result of its maximum deflection, as well as its failure shape, were compared with those of the blast experiment. Comparison of the result of the maximum midpoint deflection obtained from LS-DYNA with that of the experiment, which was reported as 68 mm, showed a 12.5% difference under the same loading condition. Figure 9 shows the failure shape of the unretrofitted CMU wall observed in the blast experiment and in LS-DYNA. As it can be seen from Figure 9, there is a good agreement between the experimental and numerical results in terms of deformation shape at failure and location of crack lines.

### 2.4.3. NPRP Retrofitted CMU Wall

In order to evaluate the soundness of the numerical models developed for NPRP retrofitted CMU walls, the simulated results were compared to the experimental results. The comparisons were in terms of the wall's maximum mid-point deflection, deformed shapes at the time of maximum deflection and at the time of wall collapse, and the location of crack lines.

The numerical simulation of the xGnP-reinforced polyurea retrofitted CMU wall model under the peak pressure of 225 kPa and an impulse of 496 kPa.msec resulted in a

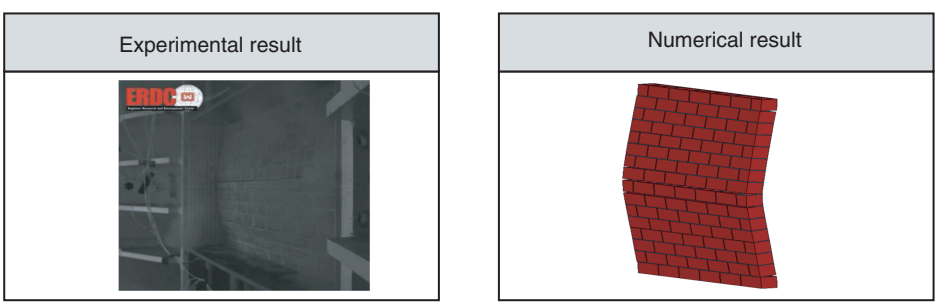


Figure 9. Response of the CMU wall subjected to a pressure equivalent to 5.44kg TNT located at 3 m in front side

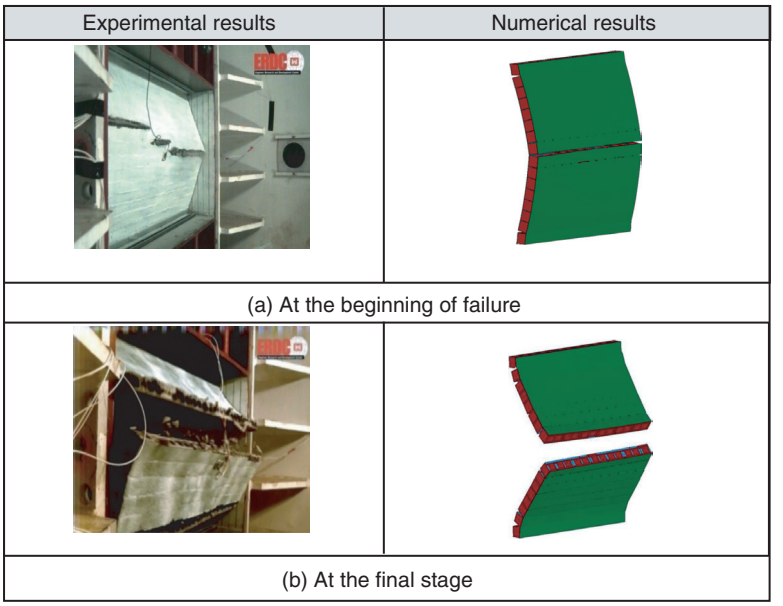


Figure 10. Deflected shape of the wall retrofitted with xGnP reinforced polyurea

maximum midpoint deflection of 82 mm. The maximum midpoint deflection obtained experimentally under the same loading condition was 76 mm. The experimental results showed that when the wall failed, the primary damage was a horizontal crack that formed over the entire width of the wall. The LS-DYNA simulation likewise showed that the wall failed by splitting into two main segments. Figure 10 illustrates the good agreement between experimental and numerical deformation shapes at the time of maximum deflection and at the end of the test.

The simulated results of the POSS reinforced polyurea retrofitted CMU wall under the peak pressure of 219 kPa and 494 kPa.msec indicated a maximum midpoint deflection of 96 mm as compared to a maximum midpoint deflection of 102 mm obtained experimentally under the same loading conditions. The experimental observation showed hairline shear and a horizontal crack at peak pressure of 219 kPa. However, the wall did not fail in either the experiment or numerical simulation analysis. Moreover, it can be seen from Figure 11 that there is good agreement between the shape of the CMU wall retrofitted with POSS reinforced polyurea obtained numerically and experimentally at the time of maximum deflection and during the final stage.

### *2.4.4. Aluminium Foam Protected CMU Wall*

The model of the aluminium foam protected wall was validated using the experimentally tested material model for aluminium foam. The details of the validation process were presented in studies by Ma (2009), and the evaluation of the validity of the unretrofitted wall model by comparison with analytical estimations, as well as experimental results, described in section 2.4.2.

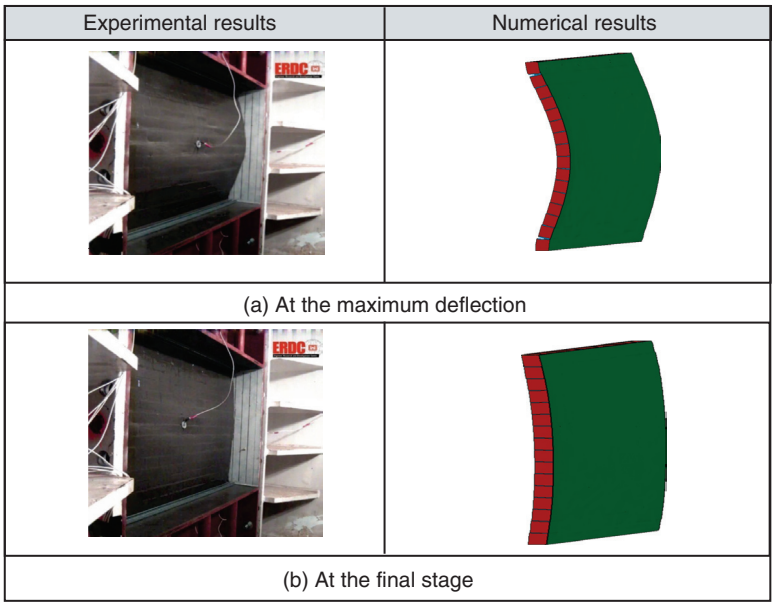


Figure 11. Deflected shape of the wall retrofitted with POSS reinforced polyurea

## 3. GENERATION OF PRESSURE-IMPULSE DIAGRAM

### 3.1. DEVELOPMENT OF PRESSURE-IMPULSE DIAGRAMS

The validated model is then used to derive pressure impulse (P-I) diagrams for the unretrofitted and retrofitted masonry walls. P-I diagrams are generated by having a certain reflected pressure ($P_r$) as a starting point. The model can then be used to predict the wall response using a small positive pressure duration ($t_d$) which is increased incrementally until a failure criterion is reached.

This process is graphically represented in Figure 12. The failure criterion was flexural failure for the purpose of generating the P-I diagrams. Once failure has been reached (first point of the P-I diagram), the model decreases the reflected pressure and repeats the process as it works through each point of the P-I diagram. The process reduces the reflected pressure incrementally, until the P-I diagram is complete.

### 3.2. DETERMINATION OF FAILURE CRITERION

In the current study, the wall performance limit state was considered to be the wall deflection at the point of collapse. Hence, each point on the curve represents a combination of pressure and impulse able to cause a wall to collapse. This criterion was selected as representing the primary damage level to be prevented. For the cases of the unretrofitted wall and aluminium foam protected wall, the deflection at instability (i.e., collapse) was estimated to be 57 mm (approximately equal to the thickness of the wall) using Eqn (7). This value was deemed to be the value of the performance limit state, and used to create the respective P-I diagrams. However, the results of tests, as well as finite element analysis, showed that the maximum wall displacement could be greater than the wall thickness when they were retrofitted with NPRPs.

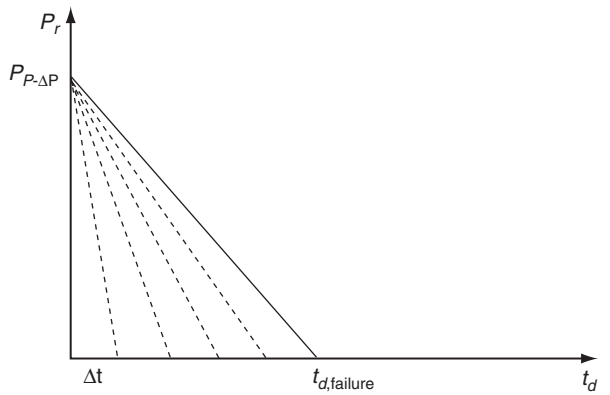


Figure 12. Maximum reflected pressure with increasing $t_d$ starting from a small value

The benefit of this noticeable flexural improvement can be attributed to the reinforced polymer retrofit. When reinforced polymer retrofitted CMU walls are subjected to blast load, the blocks near the midpoint separate initially as the tensile bond between the mortar and the masonry is weak. At first, the strain on the polymer is low. As tension increases due to increasing weakening and flexion at the joints, the spray-on polymer resists the load because of the excellent bond between the polymer and the masonry (Thornburg 2004; Dinan, Fisher, Hammons, Porter 2003). As the walls continue to deflect, the strain in the polymer at the mortar joints where cracking takes place increases until the rupture strain of the polymer is reached. Figure 13 shows the progressive failure of a reinforced polymer retrofitted CMU wall using LS-DYNA numerical simulations.

The maximum deflection Δ for the reinforced polymer retrofitted wall, where the maximum tensile strength of the polymer is reached, can be computed from Eqn (8) as recommended by Moradi, Davidson, Dinan (2008);

$$\Delta = \frac{f_t l h}{4 E_r t} \tag{8}$$

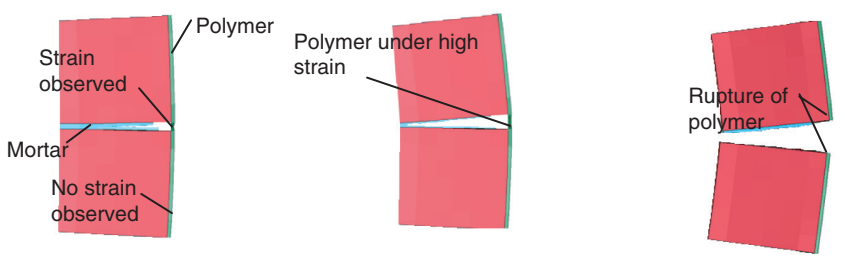


Figure 13. The progressive failure of reinforced polymer retrofitted CMU wall

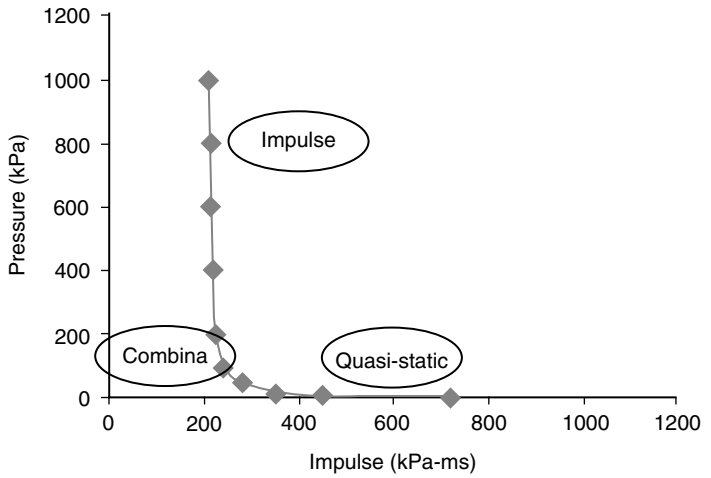


Figure 14. P-I diagram of the unretrofitted CMU wall

Here $f_t$ is the ultimate tensile strength of the polymer; $E_r$ is the polymer retrofit tangent modulus; $t$ is the wall thickness; $h$ is the wall height; and $l$ is the tributary length of retrofit.

According to Moradi, Davidson, Dinan (2008), the tributary length of the membrane affected by the crack opening is far less than the wall height, although spray-on polymer retrofit covers the entire inside surface of the wall. The tributary length depends on how the membrane retrofit is attached to the concrete masonry and how far the membrane strain extends past the crack opening (Moradi, Davidson, Dinan 2008). The LS-DYNA numerical simulation indicated that the length of NPRP retrofits strained on each side of the crack opening is generally equal to one half of the concrete masonry block height. Dinan, Fisher, Hammons, Porter (2003) also arrived at the same strain length approximation experimentally. Consequently, by assuming the approximate tributary length of the NPRP retrofit to be 27 mm and using Eqn (8), the ultimate deflection of the xGnP reinforced polyurea retrofitted wall and the POSS reinforced polyurea retrofitted wall was estimated to be 76 mm and 145 mm, respectively. These deflection values were used to generate the P-I diagrams. It should be noted that xGnP and POSS retrofit materials act as an elastomeric catcher system to prevent the masonry wall collapse before they reach the rupture strain so that noticeable flexural improvement can be achieved due to the reinforced polymer retrofit.

A P-I diagram of the unretrofitted CMU wall was created based on the performance limit state value of 57 mm as shown in Figure 14. In the impulse controlled regime, the P-I curve is near vertical, so the impulse of the blast load governs the failure of the member. Similarly, in the pressure controlled regime, the P-I curve is near horizontal, so the pressure of the blast load governs failure. In the combination regime, a combination of both the pressure and the impulse of the blast load will govern failure.

## 4. PARAMETRIC STUDIES

To obtain a better understanding of the influence of various retrofitting design factors in the effectiveness of retrofits to strengthen CMU walls, parametric analyses were conducted with the help of LS-DYNA numerical simulations. The research made use of P-I diagrams to investigate the influence of such parameters under varying pressures and impulses. The outcomes of this study can be incorporated into retrofit design.

## 4.1. INFLUENCE OF NPRP DESIGN PARAMETERS ON CMU WALL CAPACITY

Parametric studies were carried out to investigate the influence of the thickness and location of NPRPs (i.e., xGnP and POSS reinforced polyureas) on the blast resistance capacity of CMU walls. The results are summarized in the subsections below.

### *4.1.1. Thickness of NPRPs*

In order to study the effect of the layer thickness of NPRPs, the CMU walls were coated on the side away from the blast with xGnP reinforced polyureas with thicknesses of 1.5 mm, 3.0 m, or 4.5 mm. As can be seen from Figure 15, as the thickness of the xGnP increased, the P-I curve moved to the top and right of the diagram, indicating the increase in the capacity of the structure to resist the blast load. Although this improvement was considerable in all regimes, it proved more significant in situations of relatively high blast pressures with low durations. Similar results for POSS reinforced polyureas were also found.

The results of the current experimental and numerical studies demonstrated that the CMU wall would fail immediately after the rupture of the reinforced polymers. Therefore, it was possible to infer that the rupture strain of the reinforced polymers played a significant role in determining the failure of the CMU walls. Increasing the thickness of the NPRPs increased the tensile rupture capacity, as well as the strain energy absorption capacity of the polymers, which subsequently improved the blast resistance capacity of the wall.

Increasing the thickness of the NPRPs significantly improved the blast resistance capacity of the CMU walls where blast pressures were relatively high and the duration of the pressure pulses was relatively short, as opposed to low blast pressures of long duration. In other words, the higher stain rates resulted in a greater increase in the strength response of the polymers, which displayed increased resistance.

### *4.1.2. Location of NPRPs*

In order to evaluate the effect of the location of the NPRPs, finite element analysis was conducted on two different retrofit scenarios – single side retrofit, and both sides retrofit. Figure 16 shows the blast mitigation effects of the location of xGnP reinforced polyurea on CMU wall capacity. The data plots indicate that the retrofits on either a single side of

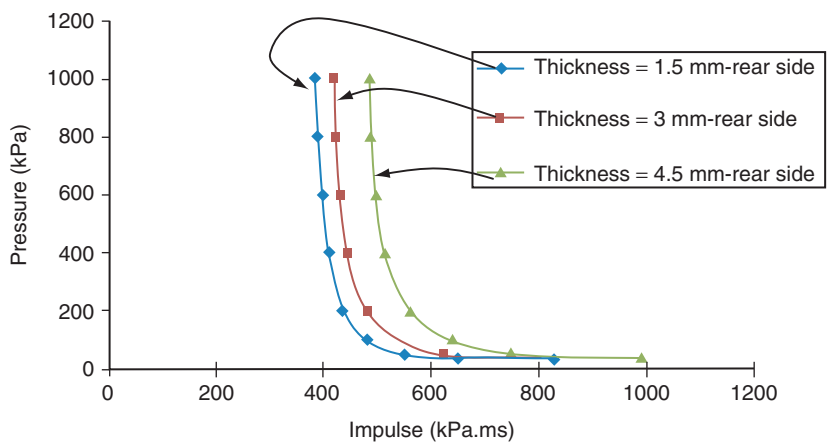


Figure 15. Influence of thickness of xGnP reinforced polyurea on CMU wall capacity

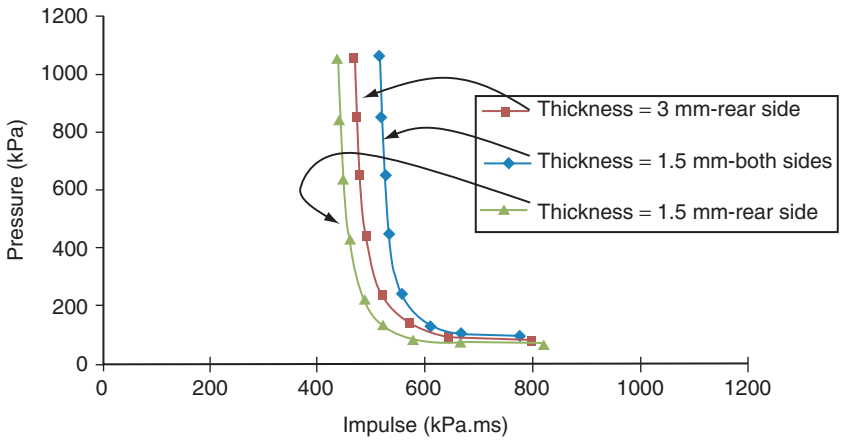


Figure 16. Influence of location of xGnP reinforced polyurea on CMU wall capacity

the wall (equivalent to the interior in this instance) or both sides improve the blast resistance capacity of the wall significantly. Similar results were also achieved for POSS reinforced polyureas.

Retrofitting the CMU wall with NPRPs on the interior side improves the blast resistance of the wall because the NPRPs allow for greater deflection and more energy dissipation through their high tensile rupture capacity. However, applying NPRPs to both sides of the wall provides the wall with more significant resistance capacity as the NPRPs on the blast side of the wall reduce or prevent CMU fracture and maintain the integrity of the wall, while the NPRPs on the interior side increase ductility. Due to strain rate effect, the impact of using NPRPs on both sides of the wall to enhance blast resistance is more noticeable in impulsive and dynamic regimes compared to quasi-static regimes.

## 4.2. INFLUENCE OF ALUMINIUM FOAM DESIGN PARAMETERS ON CMU WALL CAPACITY

A series of finite element analyses were conducted with the aid of LS-DYNA software to investigate the influence of thickness and location of aluminium foam on the mitigation of blast effects on a CMU wall. The outcomes are summarized below.

### *4.2.1. Thickness of Aluminium Foam*

In order to evaluate the effect of the thickness of the aluminium foam layer, the CMU wall was protected on the blast side with foam of various thicknesses – 13 mm, 20 mm, and 25 mm. The density of the foam was kept constant at 450 Kg/m$^3$ in all cases. As is shown in Figure 17, increasing the foam thickness helped the CMU wall to better resist the blast load. The improvement of the response of the wall as the thickness of the foam increased was more significant in a dynamic regime. Foam thickness was less important in either impulsive or quasi-static regimes.

On the whole, the thickness of the aluminium foam determined the degree of energy-dissipating deformation exhibited by the wall. The greater the deformation, the higher the energy absorption and unloading, and the less damage to the structural integrity of the wall.

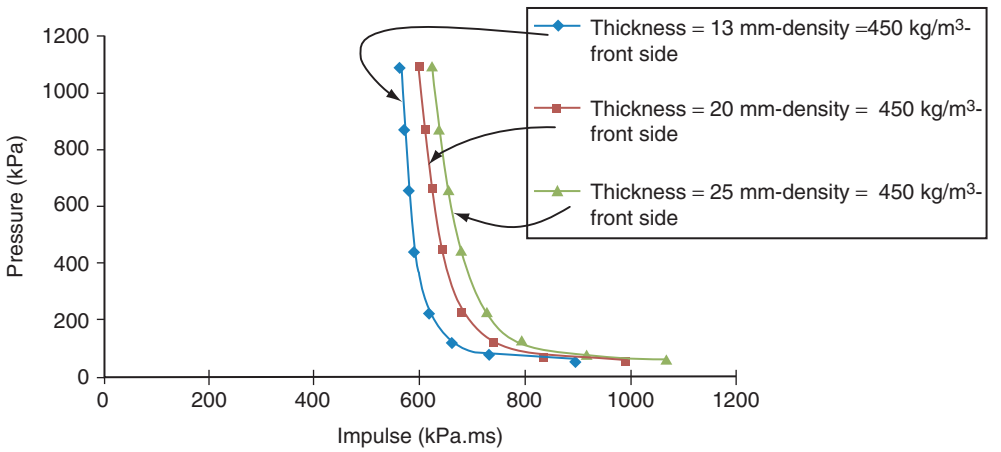


Figure 17. Influence of thickness of aluminium foam on CMU wall capacity

### *4.2.2. The Location of Aluminium Foam*

In order to investigate the effect of the location of the aluminium foam, finite element analysis was conducted on two different retrofit scenarios – retrofit on the side facing the blast, and retrofit on both sides. As shown in Figure 18, cladding the wall on both sides with the foam is the better choice when compared to using an equivalent amount of material on just the side facing away from the blast (the interior wall in this instance). The results are most pronounced for a dynamic regime. More improvement in the CMU wall resistance behavior against blast load can be achieved by cladding both sides of the wall with aluminium foam. The foam cladding on the wall facing away from a blast helps maintain structural integrity in excess of the already significant reduction in damage from the direct blast impact achieved by cladding the blast wall with aluminium foam.

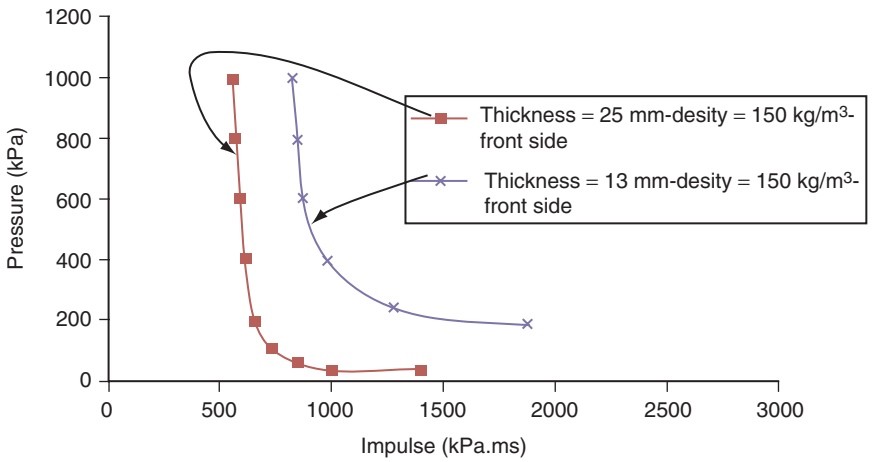


Figure 18. Influence of location of Aluminium foam on CMU wall capacity

## 5. DETERMINATION OF THE EFFICIENT RETROFITS

Ensuring the survival of a CMU wall under blast load requires selection of an efficient and expedient retrofit. The selection of the efficient retrofit depends on many factors which can be largely identified as belonging to one of two categories according to the practicality of the retrofit and the degree to which it improves the performance of the wall in the face of a blast. Clearly the ability of a wall to dissipate blast energy and resist collapse is paramount. However, retrofitting walls to attain blast resistance is neither inexpensive nor easy in many instances, and there are likely to be trade-offs. Installation involves many factors, such as getting materials into the building, handling them once inside and during installation, site preparation, safety precautions, demolition and the necessity to excavate the space. While it is acknowledged that all of these factors influence a retrofitting program, the focus of the current study was solely on the best retrofit to prevent wall collapse.

### 5.1. SPRAYED-ON POLYMERS

The P-I diagrams of unreinforced polyurea, xGnP reinforced polyurea and POSS reinforced polyurea were superimposed over each other to compare the behaviors of the polymer materials studied herein, and to determine which protected the test walls most efficiently and effectively against blast loads (Figure 19). The results of the comparison revealed that adding POSS particles to polyurea *increases* its capacity to resist blast loads. Conversely, the results showed that adding xGnP particles to polyurea clearly *decreases* its blast resistance capacity when compared to unreinforced polyurea.

While the effectiveness of the polyurea is considerable in all regimes, it is more pronounced in impulsive and dynamic regimes. The results suggest, therefore, that at relatively high pressures of short duration, POSS reinforced polyurea is the most efficient retrofit in terms of its ability to improve the resistance capacity of the wall against blast loading. However, at relatively low pressures of long duration, *all types of polyurea* are approximately of the same efficiency; and the selection of a polymeric retrofit depends largely on its practicality.

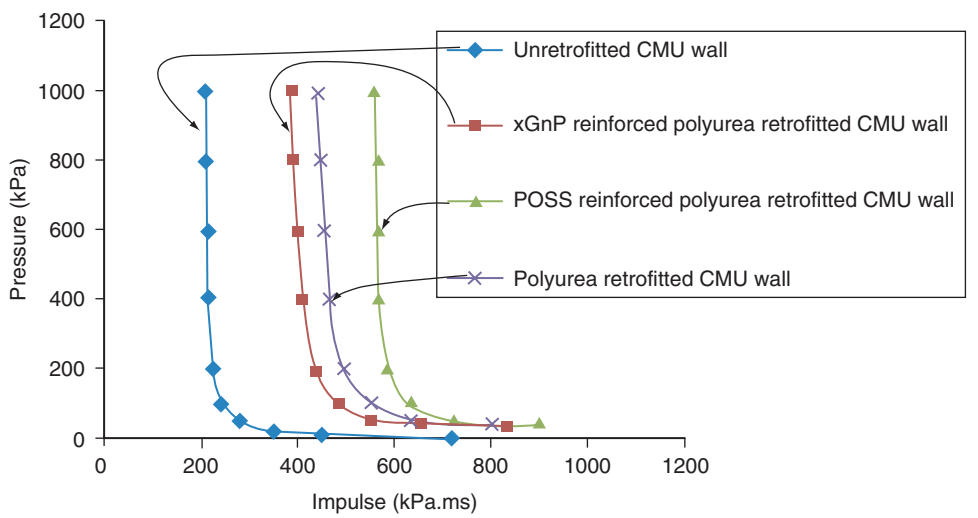


Figure 19. Comparison between the effectiveness of the three different types of sprayed-on polyurea

## 5.2. POLYMERS VS. ALUMINIUM FOAM

The POSS reinforced polyurea was compared to aluminium foam to determine whether the foam could perform as well as the reinforced polyurea. Since the thickness and location of a retrofit are the main parameters that affect efficiency, the maximum values that are practically possible were considered in order to conduct a realistic comparison of the two materials. The maximum thickness of an elastomeric material that can be applied to a wall was assumed to be 15 mm (Ward 2005), while the maximum thickness of commercially available aluminium foam is 43 mm and 450 kg/m$^3$ respectively (CYMAT 2003). These maximum values were transformed to $\frac{1}{4}$ -scale values to match the scaled geometry of the CMU walls used in this study. As Figure 20 shows, a 4.5mm thick POSS reinforced polyurea applied to the interior face of a CMU wall performed better in terms of ability to increase blast resistance capacity than 13 mm thick aluminium foam on the blast face of the wall. This difference in performance is significant, particularly in impulsive and dynamic regimes. In the quasi-static regime, both aluminium foam and POSS reinforced polyurea seemed to perform similarly, although the outcome slightly favored the aluminium foam.

Comparison between the P-I curves for an aluminium foam protected wall and a POSS reinforced polyurea protected wall where on the retrofit applies to both sides of the wall, as shown in Figure 21, revealed that when aluminium foam is applied to both sides of a CMU wall, its effectiveness is significantly increased so that it becomes the better retrofitting choice, particularly in dynamic and quasi-static regimes. However, in the impulsive regime, the POSS reinforced polyurea appeared to perform better.

Therefore, the results demonstrate that at relatively high pressures of short duration POSS reinforced polyurea is the better option in terms of boosting the blast resistance capacity of a wall compared to aluminium foam. At relatively low pressures of long duration, however, aluminium foam is generally a better choice.

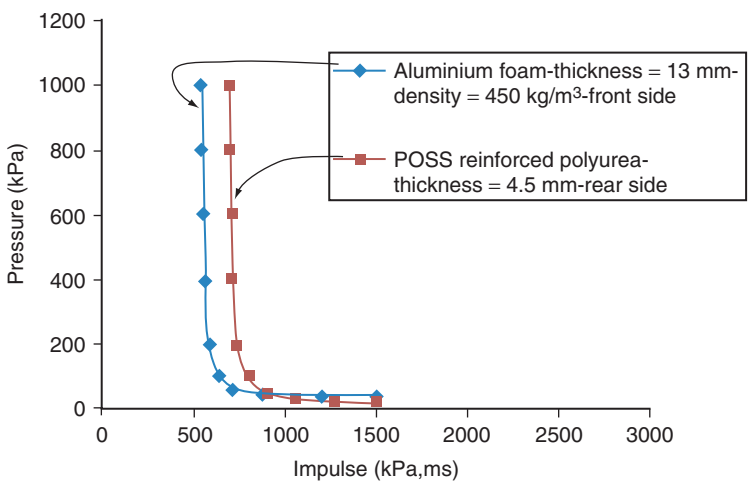


Figure 20. Comparison between the effectiveness of POSS reinforced polyurea and aluminium foam when they are applied on one side of the wall

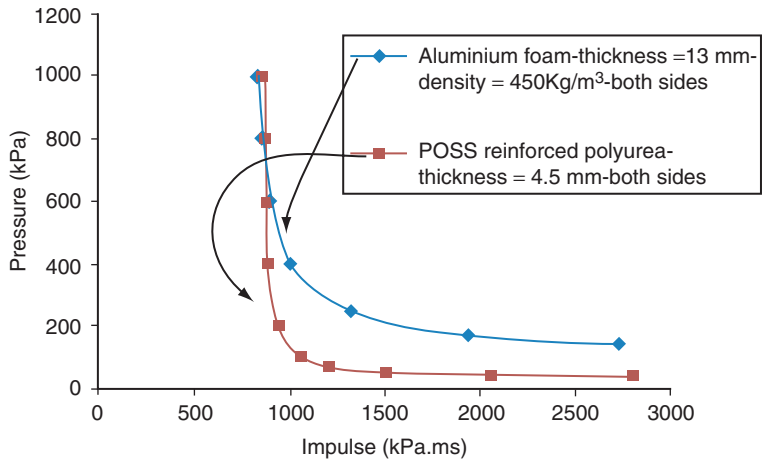


Figure 21. Comparison between the effectiveness of POSS reinforced polyurea and aluminium foam when they are applied on both sides of the wal

## 6. CONCLUSIONS

The results of this study showed that both nano-particle reinforced polymers and aluminium foam retrofits can enhance the capacity of CMU walls remarkably. The parametric studies revealed that that at relatively high pressures of short duration, POSS reinforced polyurea is the most efficient retrofit in terms of its ability to improve the resistance capacity of walls against blast loading. However, in relatively low pressures of long duration, all types of polyurea are approximately of the same efficiency. The comparison of POSS reinforced polyurea and aluminium foam showed that POSS reinforced polyurea has more capacity to enhance wall performance in the impulsive and dynamic regimes while aluminium foam is better in the quasi-static regime.

## REFERENCES

Aghdamy S. (2010). *Mitigation of blast effects on unreinforced CMU wall*. Master's Thesis, University of Adelaide, Adelaide.

Al-Ostaz A., Cheng A., Mullen C., Mantena P. R. (2009). *Nano particle reinforced composites for critical infrastructure protection*. Nano infrastructure research group, Final report, University of Mississippi.

ASCE (American Society of Civil Engineers) (1997). *Design of Blast Resistant Buildings in Petrochemical Facilities*. ASCE Task Committee on Blast Resistant Design.

Bazhenov V.G., Kibetz A.I., Kruszka L. (2012). Finite element analysis of 3-D problems of deformation and failure of masonry under explosive loading. *International Journal of Protective Structures*, 3 (4), 449–456.

CYMAT (2003). Technical Manual for CYMAT SMART METAL. Ontario, CYMAT CORP.

Davidson J. S., Fisher J. W., Hammons M. I., Porter J. R., Dinan R. J. (2005). Failure mechanism of polymer reinforced concrete masonry wall subjected to blast. *Journal of Structural Engineering*, 131(8), 1194–1205.

Davidson J. S., Moradi L. G. (2004). *Selection of a material model for simulating concrete masonry walls subjected to blast*. Interim Report, University of Alabama at Birmingham, Department of Civil and Environmental Engineering.

Dinan R. J., Fisher J. W., Hammons M. I., Porter J. R. (2003). Failure mechanisms in unreinforced concrete masonry walls retrofitted with polymer coatings: Proceeding of the 11th International symposium on interaction of the effects of munitions with structures.

Gnanasekaran D., Madhavan K., Reddy B. S. R. (2009). Development of Polyhedral Oligomeric Silsesquioxane (POSS), POSS nanocomposites and their applications: A review. *Journal of Scientific and Industrial Research*, 68, 437–464.

Griffith A. A. (1920). The phenomena of rupture and flow in solids. *Phil. Trans. Royal Soc*., London, 1920 221, 163–198.

Hanssen A. G., Enstock L., Langseth M. (2002). Close-range blast loading of aluminium foam panels. *International Journal of Impact Engineering,* 27 (6), 593–618.

Hao H., Tarasov B.G. (2008). Experimental study of dynamic material properties of clay brick and mortar at different strain rates', *Australian Journal of Structural Engineering*, 8, 2, pp. 117–131.

Irshidat M. (2010). Physics-based simulation and experiment on blast protection of infill walls and sandwich composites using new generation of nano-particle reinforced materials. PhD Thesis, The University of Mississippi, US.

Islam M. R. (2008). *Inventory of FRP strengthening methods in masonry structures*. Master's Thesis, Technical University of Catalonia, Barcelona.

Johnson C. F., Slawson T. R., Cummins T. R., Davis J. L. (2005). *Concrete masonry unit walls retrofitted with elastomeric systems for blast loads.* Proceedings for the Army Science Conference (24th).

Knox K. J., Hammons M. I., Lewis T. T., Porter J. R. (2000). *Polymer materials for structural retrofit*. Air Force Research Laboratory Air Expeditionary Forces Technology Division, FL 32403–5323.

Krishnamoorti R., Vaia R. A. (2001). Polymer nano-composites synthesis, *Characterization and Modeling*: *Proceeding of American Chemical Society*, Washington DC.

Lunn D. S., Rizkalla S. H. (2011). Strengthening of Infill Masonry Walls with FRP Materials. *Journal of Composites for Construction*, 15, 206–214.

Ma C. (2009). *Mitigation of blast effects on unreinforced masonry walls*. Master's Thesis, The University of Adelaide, Adelaide.

Montanini R. (2005). Measurement of strain rate sensitivity of aluminium foams for energy dissipation. *International Journal of Mechanical Sciences*, 47, 26–42.

Moradi L. G. (2003). Constitutive properties of a single concrete masonry unit (CMU) subjected to blast. Master's Thesis, University of Alabama at Birmingham.

Moradi L. G. (2007). Resistances of membrane retrofit concrete masonry walls to lateral pressure. PhD Thesis, University of Alabama at Birmingham.

Moradi L. G., Davidson J. S., Dinan R. J. (2008). Resistance of membrane retrofit concrete masonry walls to lateral pressure. *Journal of performance of constructed facilities*, 22(3), 131–142.

Moradi L.G., Dinan R.J., Bewick B.T., Davidson J.S. (2011). Resistance of concrete masonry walls with membrane catcher systems subjected to blast loading. *International Journal of Protective Structures*, 2 (1), 83–102.

Myers J. J. Belarbi A., El-Domiaty K. A. (2004). Blast resistance of FRP retrofitted un reinforced masonry (URM) walls with and without arching action. *TMS Journal*, 9–26.

Schenker A., Anteby I., Nizri E. (2005). Foam-protected reinforced concrete structures under Impact: experimental and numerical studies. *Journal of structural Engineering*, 131(8),1233–1242.

Stone H., Engebretsen J. (2006). The basics of blast resistant design. Proceeding of the 70th Annual Convention, Structural Engineers Association of California, 87–94.

Su Y. (2008). Numerical simulation of unreinforced masonry walls by new retrofitting technologies for blast loadings. Master's Thesis, University of Adelaide, Adelaide, 2008.

Su Y., Wu C., Griffith C. G. (2011). Modeling of the Bond-Slip Behavior in FRP Reinforced Masonry. *Construction and Building Materials,* 25*,* 328–334.

Thornburg D. L. (2004). Evaluation of elastomeric polymer used for external reinforcement of masonry walls Subjected to Blast. Master's Thesis, University of Alabama at Birmingham, 2004.

UFC (Unified Facilities Criteria) 3-340-02 (2008). *Structures to Resist the Effects of Accidental Explosions*. U.S. Army Corps of Engineers, Naval Facilities Engineering Command & Air Force Civil Engineer Support Agency (Superseded Army TM5-1300, Navy NAVFAC P-397, and Air Force AFR 88-22, dated November 1990).

Vaia R. A. (2003). Polymer nano-composites open a new dimension for plastics and composites, *AMPTIAC Newsletter*, 6(1), 17–24.

Wang M, Hao H., Ding Y., Li, ZX. (2009). Prediction of fragment size and ejection distance of masonry wall under blast load using homogenized masonry material properties. *International Journal of Impact Engineering*, 36(6), 808–820.

Ward S. P. (2005). Retrofitting existing masonry buildings to resist explosions. Masonry, <http://www.masonrymagazine.com/2-05/retrofit.html> (August 11, 2010).

Weibull W. (1951). A statistical distribution functions of wide applicability. *Journal of applied mechanics*, 18, 293–297.

Willis, C. (2004). *Design of unreinforced masonry walls for out of plane loading*. PhD Thesis, The university of Adelaide, Adelaide.

Wu C., Hao H. (2007). Safe scaled-distance of masonry infilled RC Structures to airblast loads. *Journal of Performance of Constructed Facilitie*s, ASCE 21 (6), 422–431.

Wu C., Huang L., Oehlers D. J. (2011). Blast testing of aluminium foam protected reinforced concrete slabs. *Journal of Performance for Constructed Facilities*, 25(5), 464–474.

Zhao Y., Schiraldi D. A. (2005). Thermal and mechanical properties of polyhedral oligomeric silsesquioxane (POSS)/polycarbonate composites. *Polymer*, 46(25): 11640–11647.